Quantification of the hysteresis and related phenomena in reactive HiPIMS discharges

Nikolay Britun,[1,a)] Stephanos Konstantinidis,[1] Alexandr Belosludtsev,[2,b)] Tiago Silva,[3] and Rony Snyders[1,4]
[1]*Chimie des Interactions Plasma-Surface (ChIPS), CIRMAP, Université de Mons, 23 Place du Parc, B-7000 Mons, Belgium*
[2]*Department of Physics and NTIS, University of West Bohemia, Univerzitní 8, 306 14 Plzeň, Czech Republic*
[3]*Instituto de Plasmas e Fusão Nuclear, Instituto Superior Técnico, Universidade de Lisboa, 1049-001 Lisboa, Portugal*
[4]*Materia Nova Research Center, Parc Initialis, B-7000 Mons, Belgium*

(Received 10 November 2016; accepted 5 January 2017; published online 6 March 2017)

Reactive high-power impulse magnetron sputtering discharge has been studied experimentally combining optical emission, absorption, and laser-based diagnostic techniques. The quantification of the atomic ground state densities is performed using optical emission spectroscopy. Hysteresis behavior as a function of molecular oxygen flow fraction in Ar-O_2 mixture has been observed for numerous discharge parameters, such as the ground state density of O atoms, density of the sputtered atoms and ions, Ar metastables, etc. The obtained atomic number densities are found to be in full agreement with the known models of reactive sputter deposition. The relevant plasma kinetic mechanisms influencing the measured trends are analyzed. *Published by AIP Publishing.*
[http://dx.doi.org/10.1063/1.4977819]

I. INTRODUCTION

High-power impulse magnetron sputtering (HiPIMS)[1–4] belongs to the class of so-called ionized physical vapor deposition (I-PVD) discharges.[5,6] In HiPIMS, high ionization degree of the sputtered atoms is attained as a result of narrowing the plasma pulse (typically down to 10–500 μs) with rather a low pulse duty ratio (0.5%–5%) while keeping the averaged power comparable to the level used in the direct current magnetron sputtering (DCMS) discharges. As a result, the pulse-averaged power stays normally in the kW range, discharge peak current density is in the range of 0.1–5 A/cm^2, and ionization degrees (for metal sputtering atoms) can surpass 90%.[7] HiPIMS process is highly acknowledged in the industry applications due to the unique coating properties which can be obtained, such as high film density, controllable film composition, etc.[4,8] The detailed information on the physics and applications of HiPIMS discharges for functional coating deposition is widely available in the literature.[5–7,9,10] The reactive HiPIMS (R-HiPIMS) discharges where reactive gases (such as O_2, N_2, etc.) are normally used as admixtures to the main working gas (typically Ar) for the synthesis of oxide, nitride, etc., coatings are under intense investigation nowadays.[10–12] Despite one can identify many common points between reactive DCMS[13,14] and reactive HiPIMS, the evolution of the plasma parameters in these cases is different. This happens mainly not only due to the (i) pulsed nature of HiPIMS discharge, (ii) gas rarefaction and refill phenomena,[15,16] and (iii) modified discharge current build-up mechanisms.[17]

Hysteresis is a remarkable effect appearing in reactive sputtering. In particular, this effect can be visualized as an abrupt increase of reactive gas partial pressure during the increase of reactive gas flow at some threshold point (as a result of gradual formation of compound layer on the target surface, overcoming the target cleaning), and a similar abrupt decrease of this pressure at a somewhat lower reactive gas flow (as a result of a gradual target cleaning, overcoming the compound layer formation).[18,19] The hysteresis phenomena in reactive DCMS have been investigated from both experimental[20,21] and theoretical[18,22] points of view, however, they are studied to a lesser extent in HiPIMS. So far it is known that in HiPIMS, hysteresis is narrower and sometimes barely existing, which can be beneficial for film applications as has been pointed out by Sarakinos *et al.*[23] In addition, a minimization of the hysteresis width in HiPIMS can be realized by optimizing the discharge pulse repetition rate with respect to the typical gas refill time, which is one of the most representative parameters of HiPIMS discharge, as shown by Kubart *et al.*[24]

The quantification of the densities of sputtered reactive species and their gas flow to a virtual substrate in sputtering discharges is of a special importance. This is related to the fact that the flux of these species to the film surface together with their dissociation and ionization degrees are critical for understanding the film growth as well as the target poisoning and cleaning mechanisms. In addition, better understanding of the reactive HiPIMS should enhance the process control and tailoring film stoichiometry. The particle flux towards the substrate can be determined based on the number density of the relevant species as well as their velocity or temperature. The techniques for temperature or/and velocity determination in sputtering discharges are rather well-developed,[25–27] whereas the absolute density determination remains challenging,

[a)]Author to whom correspondence should be addressed. Electronic mail: nikolay.britun@umons.ac.be
[b)]Present address: State Research Institute Centre for Physical Sciences and Technology, Physics Institute, Savanoriu ave. 231, 02300 Vilnius, Lithuania

especially for such important species as atomic O and N. The density quantification of these species during the hysteresis-related processes is especially challenging, since working in the transition zone is beneficial from the experimental point of view. After the mentioned quantification, the particle number densities (or fluxes) should potentially provide more possibilities for the advanced film growth control as well as for discharge modeling.

So far, based on the numerous intrusive and non-intrusive diagnostic methods, the metallic-to-poisoned and backward mode transitions in HiPIMS were characterized in terms of various discharge parameters including the partial pressure of reactive gas,[23] deposition rate,[28,29] discharge current and voltage,[23,24,28,30,31] relative density of the sputtered and bulk ions,[32] emission lines corresponding to reactive gas atoms,[33,34] etc. In spite of the broad range of plasma parameters studied, the current status of understanding of the hysteresis phenomena in HiPIMS suffers from two main drawbacks: (i) the lack of information on the *ground state number density* (or absolute density) of the relevant discharge species during this process, and (ii) the absence of data collected *under the same* discharge conditions. As shown recently, the O atom ground state density can be quantified in HiPIMS discharge combining optical emission spectroscopy (OES) and two photon absorption laser-induced fluorescence (TALIF) techniques.[35] At the same time, the quantification of the ground state sputtered atoms in the discharge volume is well-studied.[25,36]

Regarding this, the goal of this work was to perform a quantitative study of the hysteresis-related phenomena in reactive HiPIMS discharge under the same conditions. This goal is achieved by applying density calibration to the various studied atomic species in the discharge, including the reactive gas atoms (O in our case). The paper is organized as follows: after the description of HiPIMS setup and methodology of measurements, the studied discharge parameters are analyzed as a function of molecular oxygen flow fraction in the gas mixture. Afterwards, a brief summary and perspectives conclude the work.

II. EXPERIMENTAL SETUP AND METHODS

A. The HiPIMS discharge

The measurements have been performed in a ≈30 l stainless steel vacuum chamber with a balanced magnetron source with a 10 cm diameter circular Ti target, placed horizontally and directly cooled by ≈15 °C water flow. In this work, a reactive HiPIMS discharge operating at 20 mTorr of the working pressure in the Ar-O_2 gas mixture and having 100 Hz of a repetition frequency and 50 μs of pulse duration has been used. The gas pressure of 20 mTorr was chosen in order to obtain strong enough O TALIF signal, at the same time running HiPIMS discharge at a relatively low pressure. The pressure has been real-time controlled by a throttle valve. A schematic view of the HiPIMS reactor is given in Fig. 1, whereas the main discharge parameters are summarized in Table I. The detailed description of the mentioned sputtering reactor can be found elsewhere.[25] The typical voltage-current waveforms are presented in Fig. 2. The shown waveforms remained very similar as far as the discharge has been operating in a fixed regime (either metallic or poisoned). These

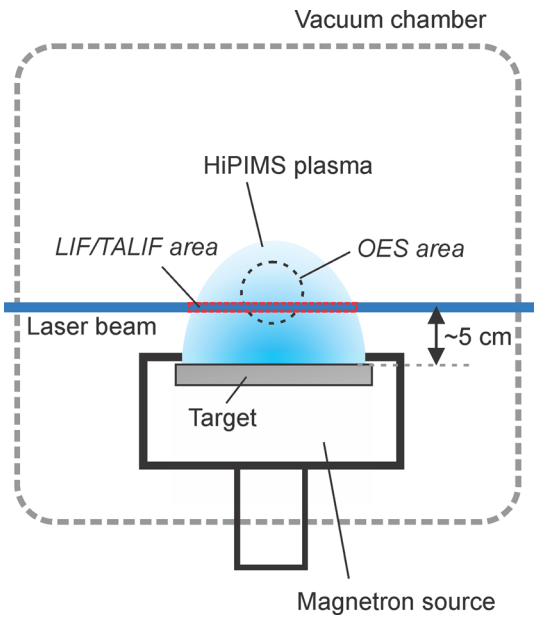

FIG. 1. Schematic side view of the studied R-HiPIMS discharge chamber with the areas of interest for LIF and OES measurements. The OES line-of-sight is perpendicular to the image plane.

waveforms reflect a typical discharge voltage and current evolution during the plasma pulse in HiPIMS case, which is related to the different spatial charge build-up mechanisms in the corresponding mode.[17] Upon the increase of the molecular oxygen flow fraction in the gas mixture, the metallic-to-poisoned mode transition typically happened at ~0.6% of the O_2 flow fraction in our case, whereas the backward transition corresponded to ~0.27%. The discharge pulse energy (E_P) was fixed at the level of ≈1 J for each experimental condition except for the power effect studies, described separately. This value corresponds to about 20 kW of the pulse-averaged applied power, and to ~0.5 A·cm^{-2} of the pulse-averaged discharge current density for our target size.

The gas flow in the HiPIMS reactor has been controlled by several calibrated digital mass flow controllers. Due to the limitations of the mass flow controllers, the total Ar + O_2 gas flow has been somewhat elevated in our work (to 100 sccm—standard cubic centimeter per minute). This has been done in order to achieve low O_2 flow fractions for the sake

TABLE I. Main parameters of the studied reactive HiPIMS discharge.

Parameter	Value
HiPIMS pulse repetition rate	100 Hz
HiPIMS pulse duration	50 μs
Working pressure	20 mTorr
O_2 flow fraction range	0.2%–40%
HiPIMS pulse energy (E_P)	≈1 J
LIF/TALIF meas. time delay	300 μs in both cases
LIF/TALIF laser beam width	≈2 mm × 5 mm/≈0.4 mm × 0.4 mm
LIF/TALIF volume of interest	10 cm^3/0.1 cm^3
LIF/TALIF photon density	~3 × 10^{13} cm^{-3}/~3 × 10^{15} cm^{-3}
Distance to target (LIF/TALIF)	≈5 cm in both cases
Laser pulse energy range	≈0.1 mJ–0.3 mJ (inside reactor)
OES measurements time delay	50 μs (end of the pulse)

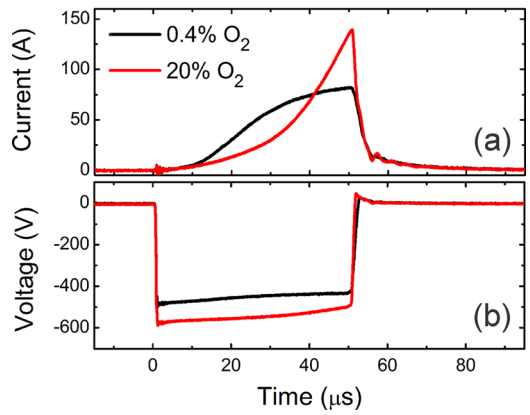

FIG. 2. Typical current-voltage waveforms taken in (a) metallic and (b) poisoned mode in the Ar-Ti-O_2 HiPIMS discharge.

of clear observation of the poisoned-to-metallic (backward) mode transition using the available mass flow controllers (see Section III C). As a result, the O_2 flow fraction in the mixture has been changing in the range of 0.2%–40%. The pumping speed at the same time has been kept constant (or nearly constant taking into account the differences in pumping speed for Ar, O, and O_2) in order to provide the constant working pressure (20 mTorr in most cases) in the discharge. The total flow rate was not changed when lower gas pressures were studied.

B. Laser-based and spectral diagnostics

Since the atomic density measurements were mainly performed during the plasma-off time (i.e., discharge afterglow), laser-induced fluorescence (LIF) technique has been implemented. Single photon absorption LIF has been used for detection of Ti and Ti^+ atoms, whereas two-photon absorption LIF (TALIF) was applied for O ground state atom detection. These measurements were performed according to the well-known atomic excitation as well as the signal detection schemes, available in the literature for both LIF[25] and TALIF[37] techniques. The summary of the optical transitions used in our case can be found in Table II.

The laser-based measurements have been performed using a pulsed Sirah dye laser with ~5 ns of the pulse duration and 10 Hz of repetition frequency. The volume of interest was located at about 5 cm above the target surface (see Fig. 1). An Andor iStar740 DH740-18F series intensified charge coupled device (ICCD) camera bundled with a Nikkor 50 mm imaging lens (at the aperture f/1.4) has been used as a detector. The laser pulse energy (E_{las}) has been continuously monitored during the measurements followed by normalization of the measured LIF (TALIF) signal by E_{las}^{S} ($E_{las}^{2\gamma}$), where S (γ) are the parameters of nonlinearity with respect to the laser energy. More details on laser energy normalization can be found elsewhere.[10,25,38] In the case of TALIF diagnostics of O ground state atoms, the optical band pass filter at 840 nm (with an optical width of 10 nm) has been utilized. The resulting signal in this case was represented by the Ar and O emission lines, with Ar lines' contribution exceeding 90% at the end of the plasma pulse, as illustrated in Fig. 3. Such a strong plasma emission made the TALIF measurements impossible during the plasma pulse, and required a careful background separation at the beginning of the afterglow time.[35]

The optical emission spectroscopy (OES) measurements have been performed using a visible-infrared optical fiber connected to an Andor SR750 spectrometer coupled with mentioned ICCD detector. During these measurements, the signal was averaged along the line-of-sight (perpendicularly to the image plane in Fig. 1). The focal length of the spectrometer was 0.75 m providing a resolution of about 0.05 nm (at 500 nm). The OES measurements, both related to the actinometry and to electron temperature determination, were performed using the emission spectra corrected by the spectral response of the "fiber + monochromator + ICCD" system.

C. Number density calibration

1. Ground state O

The measurements of the number density of O ground state atoms by OES technique have been realized using the so-called optical emission actinometry. These measurements were performed at the end of the plasma pulse (i.e., at 50 μs). The actinometry method was successfully applied recently in a middle-pressure microwave discharge for diagnostics of CO absolute density,[39] and its basics are available in the literature.[40] Here only the basic expressions are given.

Having a plasma discharge operating in the mixture of gases (Ar-O_2 in our case), one of the gases with the known

TABLE II. Summary of the spectral transitions used for HiPIMS discharge diagnostics.

Measured quantity	Technique used	Atomic state	Nature of atomic state	Transition wavelength (nm)[43]
Ti density	LIF[25]	$3d^24s^2\ a\ ^3F_2$	Ground	320.58 (excitation)/508.70 (fluorescence)
Ti^+ density	LIF[25]	$3d^2(^3F)4s\ a\ ^4F_{3/2}$	Ground	314.80 (excitation)/456.38 (fluorescence)
O density	TALIF[38]	$2s^22p^4\ ^3P_2$	Ground	225.58 (excitation)/844.6 triplet (fluorescence)
O density calibration	OES[35]	O: $2s^22p^4\ ^3P_2$	Radiative (excited)	O: 777.19
		Ar: $2p_1$, $2p_2$, $2p_3$, $2p_5$		Ar: 750.39, 826.45, 727.29, 696.54, 840.82, 738.40, 706.72, 751.47
Ar $1s_x$ density	AAS[36,a)]	$1s_5$, $1s_4$	Metastable + Radiative	810.37, 811.53
O (metastable) density	AAS[47]	$3s\ ^5S^o_2$	Metastable	777.19, 777.42, 777.54
Ar emission	OES	$2p_1$–$2p_8$	Radiative	750.39 + other lines (totally 13)
O emission	OES	$3p\ ^5P_3$	Radiative	777.19
Electron temperature	Ar line ratio[45]	…	…	425.94, 750.39

[a)]AAS stands for Atomic Absorption Spectroscopy

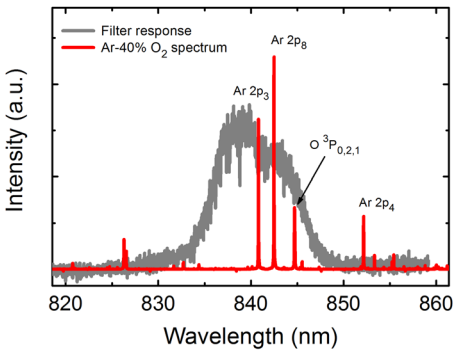

FIG. 3. Spectral response of the optical bandpass filter (840 nm of central wavelength, 10 nm of the bandwidth) used for TALIF signal detection in this work. The emission spectrum (red line, taken at the time delay = 50 μs and ICCD gate width = 2 μs) is given for comparison. The upper states of the relevant Ar and O transitions are indicated.

concentration can be used as actinometer, whereas the number density of the other gas can be determined based on the ratio of the corresponding emission lines. In case when O atom density should be determined and Ar serves as the actinometer, the ground state atom densities of these gases and the ratio of their emission lines are related to each other

$$\frac{n_{GS}^{O}}{n_{GS}^{Ar}} = \frac{I_{ij}^{O}}{I_{ij}^{Ar}} \frac{\lambda_{ij}^{O}}{\lambda_{ij}^{Ar}} \frac{A_{ij}^{Ar}}{A_{ij}^{O}} \frac{k_i^{Ar}}{k_i^{O}} \frac{\sum A_{ik}^{O}}{\sum A_{ik}^{Ar}}, \quad (1)$$

where n_{GS}^{O} and n_{GS}^{Ar} are the ground state number densities of O and Ar, respectively, $\frac{I_{ij}^{O}}{I_{ij}^{Ar}}$ is the ratio of their emission lines corresponding to the spectral transition from i to j level, λ_{ij}^{O} and λ_{ij}^{Ar} are the corresponding wavelengths, A_{ij}^{O} and A_{ij}^{Ar} are the coefficients of spontaneous emission, k_i^{O} and k_i^{Ar} are the electron impact excitation coefficients corresponding to excitation from the ground state to the upper level i, and $\sum A_{ik}$ are the total radiative de-excitation loss from the upper level i. Expression (1) derived assuming (i) the population of the upper levels happens solely by excitation from the ground state, neglecting the contribution of intermediate (e.g., metastable) states, and (ii) the collisional quenching of the state i is negligible. The first assumption is valid in our case based on the estimations of contribution of Ar metastable and radiative $1s_x$ states following the study of Boffard *et al.*,[41] whereas the second assumption is generally valid in low-pressure discharges, as the radiative de-excitation of the radiative (i.e., non-metastable) states dominates in this case. Writing the expression (1) for O ground state atom density, we obtain

$$n_{GS}^{O} = n_{GS}^{Ar} R^{O/Ar} \frac{\lambda_{ij}^{O}}{\lambda_{ij}^{Ar}} \frac{A_{ij}^{Ar}}{A_{ij}^{O}} \frac{k_i^{Ar}}{k_i^{O}} \frac{\sum A_{ik}^{O}}{\sum A_{ik}^{Ar}}, \quad (2)$$

where $R^{O/Ar}$ stands for the O to Ar emission line ratio, which should be determined experimentally. In our case, the Ar ground state density was estimated according to ideal gas laws, the ratio of the excitation coefficients was calculated based on the electron impact cross section data available in the literature,[42] and the other spectral parameters were taken from the corresponding databases.[43,44] Seven Ar emission peaks were used for O atom density calculations producing the relative error of about 50%. The actinometry data have been used for calibration of O TALIF signal obtained as a result of measurements in the afterglow. More details on O atom density calibration are available elsewhere.[35]

2. Ground state Ti and Ti^+

Another Ar-Ti HiPIMS discharge (working at 1 kHz of repetition rate, at 20 mTorr of working pressure, and having 20 μs of the pulse duration and 0.3 J of the pulse energy) has been used for Ti and Ti^+ density calibration purpose. The number densities of the sputtered Ti neutrals and ions were calibrated comparing the optical absorption spectroscopy results obtained previously[36] with the LIF measurements performed under the mentioned conditions in this work, thus letting us to apply the LIF measurements in the studied reactive HiPIMS discharge. The calibration has been performed at about 5 cm above the target, as in the case of TALIF measurements. The actual time delays and the corresponding absolute Ti and Ti^+ densities used for calibration are shown in Fig. 4(a). The calibration has been performed at the very end of the discharge afterglow (900 μs of time delay) due to the uniformity of the Ti and Ti^+ ground state density distributions achieved at this time (see Figs. 4(b) and 4(c)) as confirmed by LIF imaging.[25] The high spatial uniformity is important for calibration since under this condition, the LIF measurements (which are local) should give the values close to those measured by absorption spectroscopy (line-of-sight technique). The spectral details on the optical absorption measurements for Ti and Ti^+ are listed in Table II, as well as can be found elsewhere.[36]

D. Electron temperature determination

The electron temperature (T_e) is an important parameter for O atom density calibration procedure by optical emission actinometry, as the ratio of the electron impact excitation coefficients for O and Ar excited states, is sensitive to this quantity.[35] Due to this fact T_e has been additionally measured at the time delay corresponding to the O atom density calibration (50 μs) under several discharge conditions and used for further O density calibration, as mentioned above. The electron temperature has been determined by the Ar line ratio according to the method proposed by Silva *et al.*[45] using the expression

$$T_e = \left(7.04 \cdot N(1s_5)^{0.10}\right) - \mathrm{Log}\left(\frac{0.19}{R} - 1\right) \Big/ \left(6.03 - 17.86 \cdot N(1s_5)^{0.17}\right), \quad (3)$$

where R is the intensity ratio for Ar 425.9 nm and 750.4 nm emission lines (corresponding to the Ar $3p_1 \rightarrow 1s_2$ and $2p_1 \rightarrow 1s_3$ transitions, respectively), $N(1s_5)$ is the population of Ar $1s_5$ metastable state normalized to the Ar ground state density. The Boltzmann distribution over the Ar $1s_x$ states is assumed in this case. The relative error of T_e obtained by formula (3) is estimated to be about 10%.[45] This error is mainly

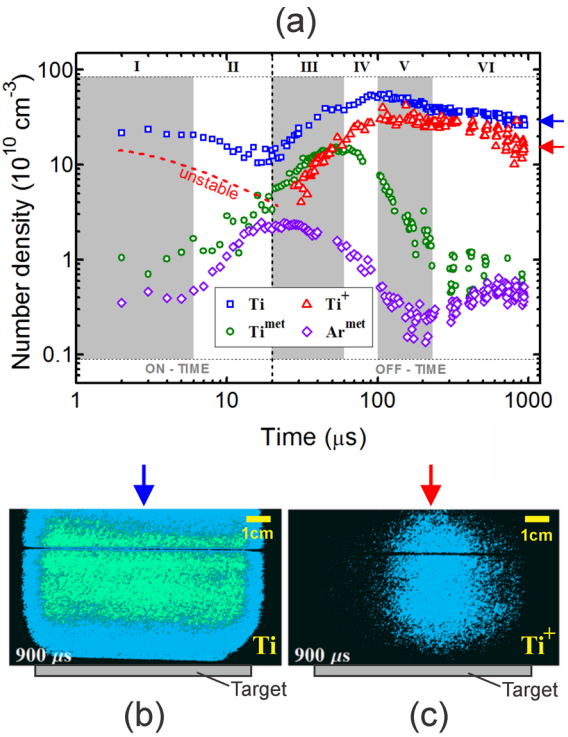

FIG. 4. (a) Time-resolved evolution of the atomic species in a 1 kHz Ar-Ti HiPIMS discharge (used for the calibration purpose) measured by absorption spectroscopy. The calibration points for Ti and Ti^+ are indicated by arrows. Reproduced with permission from J. Appl. Phys. **117**, 163303 (2015). Copyright 2015 AIP Publishing. (b) Ti neutrals and (c) Ti ion 2-D density distributions above the target measured by LIF imaging at the end of the plasma off-time (900 μs after the pulse start) in the same HiPIMS discharge. The ICCD gate widths are 2 μs (a) and 20 ns (b) and (c).

defined by the uncertainties of the emission line measurements, but not by the assumptions made (i.e., the electron excitation from the ground state and metastable ($1s_x$) states of Ar). The population of the Ar $1s_5$ metastable state was taken into account in our case while calculating the electron temperature, since this state might play an important role in population of the upper (3p, 4p,.) Ar states, affecting T_e determination by the proposed method. The obtained electron temperature values are grouping around 2 eV for the wide variety of the examined discharge conditions (see Sec. III C), barely depending on the target material, as shown recently.[35]

III. RESULTS AND DISCUSSION

A. General O density trends

The emission spectra of the Ar-Ti-O_2 HiPIMS discharge in the metallic and poisoned (oxidized) modes of operation are given in Fig. 5. The dramatic decrease in the emission intensity for the lines corresponding to Ti (300–550 nm range) and Ti^+ (e.g., around 336 nm) excited states as a result of transition to the poisoned mode is evident. To the contrary, an increase in the emission intensity from the selected Ar and Ar ion peaks is clearly observed. In the poisoned mode, the appearance of the O atomic spectral lines is also evident (mainly around 777 nm and 845 nm, shown by green arrows), even though the intensity of these lines is small in the presented scale. The observed changes correspond to the dramatic decrease of the sputtering yield in poisoned mode as confirmed by the following results. Indeed, as a result of metallic-to-poisoned mode transition, the sputtering yield for metal atoms decreases[17,19] together with their density in the plasma volume. Thus, much weaker intensity of the corresponding emission lines is expected, as the electron density (mainly represented by secondary electrons) is roughly comparable in the metallic and poisoned modes in the Ti case.[46]

As suggested in the studies related to the atomic oxygen dynamic in reactive HiPIMS undertaken so far,[35,47,48] the atomic oxygen may be generated during the plasma pulse as a result of several pathways, including the dissociation of O_2 in the plasma bulk ($O_2 + e \rightarrow O + O + e$), dissociation of the O-containing sputtered compounds (TiO, TiO_2, etc.) passing through the ionization zone (e.g., $TiO + e \rightarrow Ti + O + e$), direct sputtering of O atoms, etc. The electron impact dissociation is supposed to be the main mechanism for O atom production during the plasma pulse, giving the abundance of bulk O_2. At the same time, during the HiPIMS afterglow, the diffusion of O atoms and their recombination with the other species (usually negligible in the plasma bulk) as well as with the

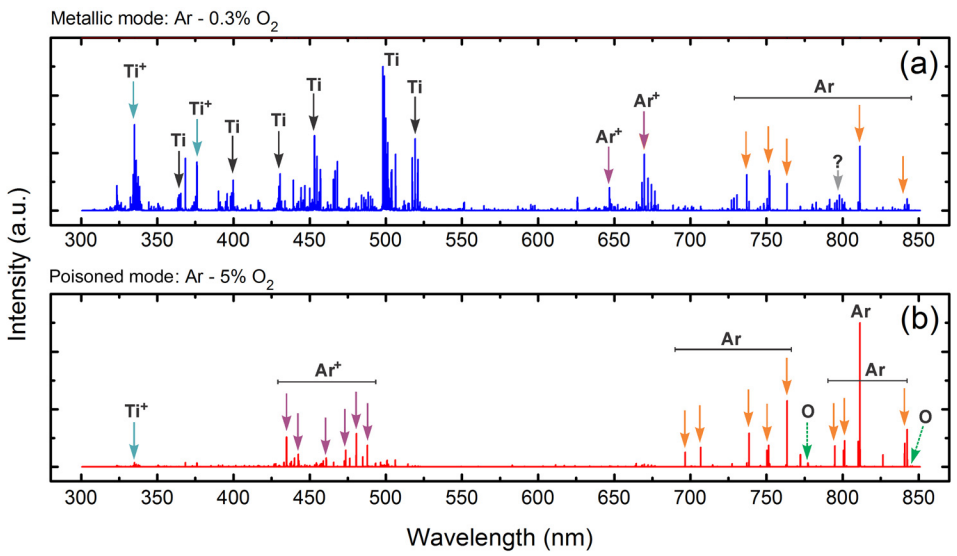

FIG. 5. The emission spectra taken at the end of the plasma pulse (50 μs) in the Ar-Ti-O_2 R-HiPIMS discharge in the (a) metallic and (b) poisoned mode. The characteristic emission lines are indicated by arrows. The ICCD gate width = 2 μs.

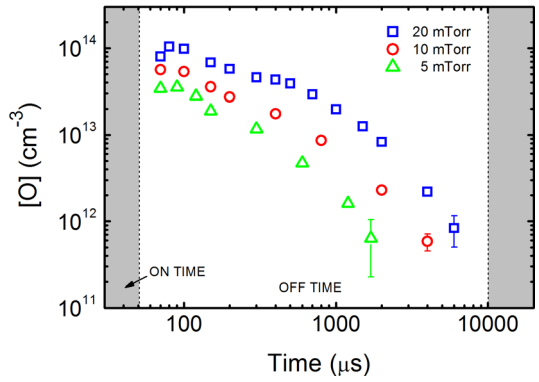

FIG. 6. Time-resolved distributions of the O atom ground state density during the R-HiPIMS afterglow at three working pressures. The data are measured by TALIF and calibrated by OES technique (see text). O_2 flow fraction is 40%.

chamber walls should be considered, resulting in a quick O density decay (i.e., $O + X \rightarrow XO$, with X being either O or Ti atom; and $O + wall \rightarrow O_{adsorbed}$). The result of these processes measured by TALIF technique during the HiPIMS afterglow is presented in Fig. 6 for three different discharge pressures. As mentioned earlier, the calibration uncertainty in this case is ~50% (which is also valid for the O density results shown below). As one can see, the total decay in O density in this case exceeds two orders of magnitude during ~10 ms of the afterglow time. The decay rates are comparable for the considered gas pressures. The O atom density is also strongly pressure dependent, increasing proportionally to this parameter. Somewhat decelerated O atom density decay appearing at about 500 μs (see Fig. 6), which is especially noticeable at 20 mTorr might be a result of O_2 decomposition by the Ar metastables ($O_2 + Ar^{met} \rightarrow O + O + Ar$) which start to refill the volume of interest during this time.[25] The shown O atom density dynamics correlates very well with results found for the other sputtered metals.[35]

B. HiPIMS pulse energy effects

Let us briefly consider the power-induced changes in the O atom density. The changes in the energy E_P supplied to a HiPIMS plasma pulse (which is proportional to the applied power) affect the behavior of the ground state O atoms differently. The corresponding results are given in Fig. 7, where the changes in the number densities of the ground state O, Ti, and Ti^+ depending on E_P are presented. In this case, all the measurements were performed in the HiPIMS discharge afterglow at a time delay of 1 ms (i.e., 950 μs after the plasma pulse). Several observations can be made based on the presented data. First, the O density in the metallic mode is barely detectable, so no power-related trend can be built (the estimations are given below). There is a clear increase in the O atoms density in the poisoned mode, however. Fitting the obtained data in the entire examined range, a nearly 2.5 fold overall increase in the O density can be deduced, when E_P increases roughly 6 times. Second, the Ti neutral density is almost non-sensitive to the pulse energy in the metallic mode (changing by only about 20%) and totally non-sensitive in the poisoned mode. Finally, the Ti ion density demonstrates a much higher sensitivity to E_P compared to Ti neutrals, changing by a factor of ~2 in the metallic mode and nearly fivefold in the poisoned mode. Note that transition to the poisoned mode accompanied by a dramatic O density drop may happen if the pulse energy is too low ($E_P < 0.6$ J in our case). Such transitions in case of Ti and Ti^+ are shown by the dashed arrows in Fig. 7.

Based on these observations, we can conclude that only the Ti ion density in poisoned mode is directly proportional to the plasma pulse energy. In the other cases, the number density responses to the pulse energy changes are weaker. The behavior for Ti and Ti ions in metallic mode is expected, as the number of the produced metal particles, both neutrals and ions, stays weakly proportional to the applied power. In the poisoned mode, as a result of a dramatic decrease in metal atom sputtering yield, Ti density drops significantly (>20 times in our case, compare Figs. 7(c) and 7(d)), and Ti is likely produced mainly as a result of Ti-compound dissociation (e.g., $TiO + e \rightarrow Ti + O + e$). This mechanism should be rather weak though, the Ti density does not react to the E_P variations (Fig. 7(d)). On the other hand, the O atom density increases with E_P, pointing out to the other source of O production, which might be the dissociation of O_2 (primarily, since O_2 is abundant) or non-binary compounds, which would favor the production of O atoms without the production of Ti (e.g., $TiO_2 + e \rightarrow TiO + O + e$). This process is likely related to the increase of electron density in the ionization zone with increasing of the pulse energy, which also explains the observed fast growth of Ti^+ density proportional to E_P. In this case, the Ti ion production should happen almost solely as a result of the ionization of the plasma bulk Ti ($Ti + e \rightarrow Ti^+ + 2e$) which remains non-sensitive to the E_P changes. The ionization by Penning mechanism ($Ti + Ar^{met} \rightarrow Ti^+ + Ar$) might also be essential in the afterglow during this time (500–1000 μs), as it corresponds to refilling of the volume of interest by Ar metastables, as mentioned above. Note, that the Ti ionization degree is equal to only about 2% in this case (see Figs. 7(d) and 7(f)). The increase in O atom density can also be due to the enhanced dissociation of the sputtered compounds in the plasma volume, as their sputtering rate increases at higher E_P. Future discharge modeling, taking into account the relevant kinetics and corresponding cross section data, should further clarify these suggestions.

C. Hysteresis effects

1. Discharge current, Ti ionization, etc.

Let us finally consider the hysteresis-related effects. First of all, the behavior of the discharge peak current (see Fig. 2) demonstrates a clear increase when switching to the poisoned mode. It is known that in the case of Ti-based reactive HiPIMS, the current shape is mainly defined by a comparable contribution of Ti and Ar ions in the metallic mode,[49] showing rather moderated current values. In the poisoned mode, the current evolution is retarded due to the presence of the compound layer on the target surface and the whole process changes to Ar^+-dominated sputtering with a little contribution of O^+ producing much higher *peak* current values at the end of

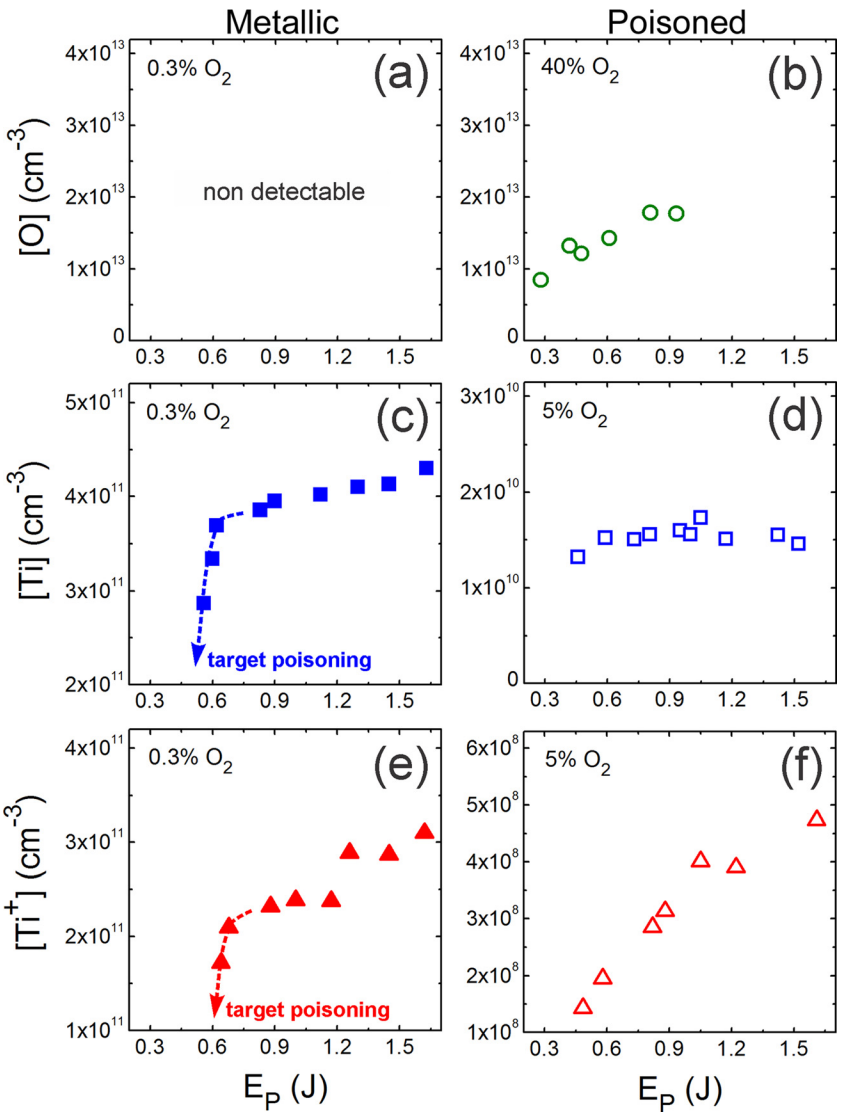

FIG. 7. The number density of O atoms (a) and (b), Ti neutrals (c) and (d), and Ti ions (e) and (f) measured by LIF and calibrated accordingly as a function of the R-HiPIMS pulse energy E_P. The data are given in both metallic (a), (c), and (e) and poisoned (b), (d), and (f) discharge regimes. The O_2 flow fraction is given in the left upper corners. The transitions to poisoned mode due to the target contamination are additionally indicated by arrows.

the pulse,[11,17] which is recently confirmed by modeling.[49] The role of O_2 dissociation assisted by an immediate O ionization giving two O^+ ions might be an essential mechanism in this case as well ($O_2 + e \rightarrow 2O + e$, followed by $2O + 2e \rightarrow 2O^+ + 4e$).[50] The result of these processes is shown in Fig. 8(a) where the peak current behavior clearly defines the hysteresis width, corresponding to ~0.27%–0.6% range of the O_2 flow fraction in our case. The voltage data give similar results (not shown here). Figs. 8(b) and 8(c) show the hysteresis-like dynamics for the Ti and Ti^+ number density as well as for the Ti ionization degree η in the volume of measurements (defined as $\eta = [Ti^+]/([Ti] + [Ti^+])$, where [] stands for ground state density). As we can see, both [Ti] and [Ti^+] reveal the hysteresis behavior, demonstrating a more than one order of magnitude jump as a result of transition to the poisoned mode. Further increase of the O_2 flow fraction does not alter the Ti density significantly, whereas [Ti^+] drops continuously, by nearly three orders of magnitude in the examined $\%O_2$ range, resulting in a similar drop of η. The obtained η values are equal to about 0.4 in the metallic mode which is comparable to the values from the literature.[36,51] Moreover, a clear hysteresis-like behavior is absent for η.

2. Ground state O atoms

The dynamics of the O atom density and its hysteresis behavior represents one of the main goals of this study. The calibrated O atom density clearly reveals hysteresis (see Fig. 8(d)), demonstrating a linear density increase in the poisoned mode with an addition of O_2 to the gas mixture (in the log-log scale). Unfortunately, the O atom density values approached the detection limit in the metallic mode in our case, sometimes producing >100% of the relative error (several independent TALIF measurements are averaged for the data points presented in Fig. 8(d)). This does not include the O density calibration error. In this regard, the presented O atom density values in the metallic mode can be considered as rough estimations only (density level is estimated to be in the range of 10^{11}–10^{12} cm^{-3}). In spite of this fact, the mode *transitions* are clearly detected experimentally for both metallic-to-poisoned and poisoned-to-metallic transitions cases. We should also emphasize that the overall behavior of O atom density found in our work is in total agreement with the early modeling done by Berg *et al.*,[18] as well as with later works.[13,14]

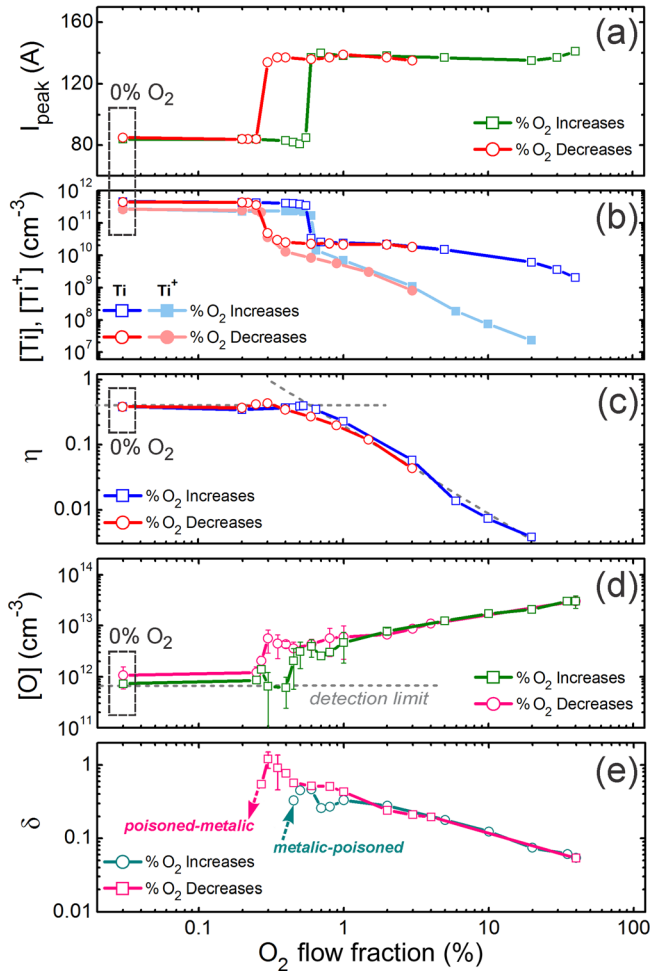

FIG. 8. O_2 flow fraction-dependent behavior of the following quantities in the R-HiPIMS discharge: (a) discharge peak current, (b) Ti and Ti^+ ground state density, (c) Ti ionization degree η, (d) O atom ground state density, and (e) δ (see text). Time delay is 300 μs (except for (a), where it is ~50 μs).

Some attention should also be devoted to the dissociation degree of molecular oxygen. There are three main pathways for sinking the reactive gas molecules during reactive sputtering, namely, the gettering by target, adsorption on the walls, and pumping of the remaining bulk molecules.[18] For a proper determination of the local O_2 dissociation degree, the *in-situ* measurements of the absolute ground state density of O_2 in the volume of TALIF measurements should be undertaken. In this case, the dissociation degree of O_2 can be rigorously defined as $1/2\,[O]/[O_2]$. This is valid if the O_2 dissociation can be assumed as a main mechanism for O atom production in the plasma bulk. Since the $[O_2]$ measurements were not performed locally in our case, and the relative contribution of O production mechanisms requires additional verification, only an estimation based on the injected density of molecular oxygen can be made. In this case, the quantity $\delta = 1/2\,[O]/[O_2]_{inj.}$ can be introduced, giving a similar ratio between the locally measured O density, and O_2 density defined via the injected O_2 flow. The obtained δ values as a function of the O_2 flow fraction are given in Fig. 8(e). In this case, the data for metallic mode are excluded, since a nearly zero partial pressure of O_2 is expected in the plasma volume due to gettering.[18]

In order to compare the presented δ values to the real O_2 dissociation degree, the correct estimation of the O_2 partial pressure in the volume of interest should be performed. There are few obstacles, however, for this estimation, such as (i) the difference in O_2 partial pressure in the reactor with and without the presence of the discharge, (ii) the role of the walls, (iii) the rarefaction in HiPIMS. Even if the effects of the partial pressure change (negligible in our case, as verified additionally), as well as the wall adsorption effect (not verified) can be ignored, the rarefaction effect may introduce rather essential changes in the local gas pressure, which cannot be accounted globally (i.e., using the ideal gas laws). Since the rarefaction in HiPIMS is especially pronounced up to 1 ms after the plasma pulse[25,36,52] it can lead to a pressure drop up to one order of magnitude, according to the theoretical estimations done by Vlček *et al.*[53] As a result, the question about precise calculation of the O_2 dissociation degree remains open. The local *in-situ* measurements of the O_2 ground state density combined with O density determination should be the most efficient approach to clarify the O_2 dissociation dynamics experimentally. At the same time, the data presented in Fig. 8(e) may indicate the global trends of O_2 dissociation, assuming that the relative contributions of the factors influencing O production as well as O_2 disappearance do not change much in the poisoned mode.

3. Electron temperature, excitation, and related parameters

As shown in Fig. 9(a), the combined density of the Ar $1s_5 + 1s_4$ states also reveals hysteresis-like behavior, demonstrating about a threefold increase during the metallic-to-poisoned mode transition. This may reflect the general trends for sputtering in poisoned HiPIMS regime, where the Ar ion-dominated sputtering prevails.[17] Recent modeling of the reactive HiPIMS plasma pulse shows that the electron density at the end of the HiPIMS plasma pulse may be twice higher in the poisoned mode.[49] Thus, the combination of Ar^+-dominated sputtering combined with potentially higher electron density at the end of the plasma pulse results in the higher density of Ar metastables in the poisoned mode within the hysteresis zone. This fact may increase the O_2 production in this region as observed in Fig. 8(d). The effect of Ar metastables on O_2 dissociation in the afterglow should be more pronounced due to the lower threshold energy of this process (~5 eV (Ref. 54)), compared to the Ti ionization (~6.8 eV). This fact likely defines a much steeper decay for η (Fig. 8(c)), compared to δ (Fig. 8(e)).

The production of both O atoms and Ti ions during the plasma pulse is mainly defined by electron excitation, as Penning ionization by Ar^{met} is negligible during the HiPIMS pulse.[55] The behavior of the electron temperature shown in Fig. 9(b) (estimated based on the line ratio method taking into account the Ar metastable density data from Fig. 9(a)) resembles a hysteresis loop in our case, although without a well-defined transition zone. As we can see from Fig. 9(b), T_e remains somewhat lower in the metallic mode and gets higher in the poisoned mode. No abrupt jump of T_e is observed. This might be related to rather a high relative error

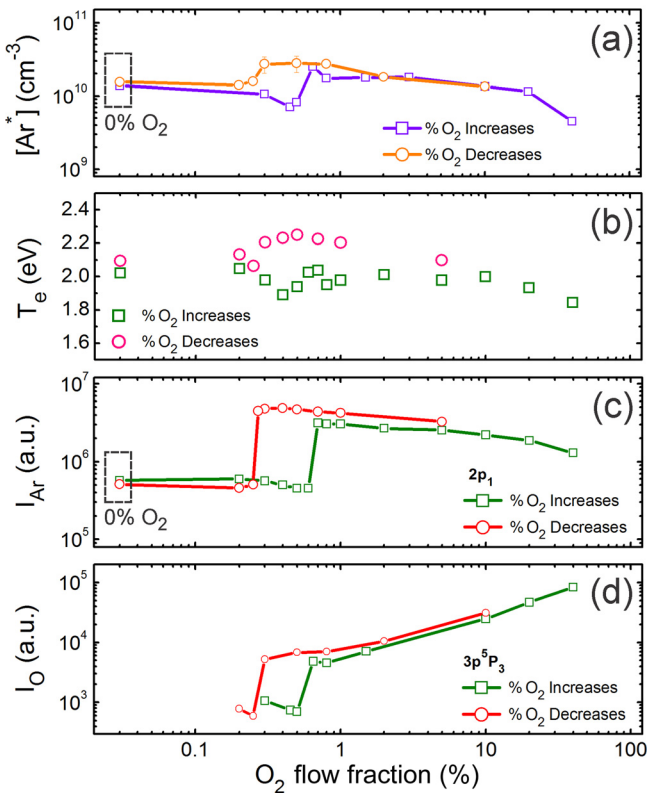

FIG. 9. O_2 flow fraction-dependent behavior of the following quantities in the R-HiPIMS discharge: (a) Ar ($1s_5 + 1s_4$) number density, (b) electron temperature, (c) Ar emission line intensity, and (d) O emission line intensity. The upper states for the emission lines are indicated. Time delay is 50 μs.

of these measurements (higher than ~10% estimated previously[45]), due to the large uncertainty in the measurements of the Ar^{met} density as well as in the 425.9 nm Ar emission line in our case. The values of T_e found in this work are in a reasonable agreement with the values experimentally measured (by Langmuir probe) at the end of the HiPIMS plasma pulse,[56,57] albeit contradicting the recent modeling results.[49]

The found T_e behavior may be important for explanation of the higher Ar^{met} density as well as higher O_2 dissociation in the poisoned mode within the hysteresis zone. Indeed, the changes in T_e observed in our case (~0.5 eV) should induce rather essential changes in the high energy tail of the electron energy distribution, which may alter the O_2 dissociation significantly. This represents another subject for the future studies. The monotonous decrease in T_e registered between 1% and 40% of the O_2 flow fraction may be the result of electron energy absorption by the additional (rotational and vibrational, easy to excite) degrees of freedom of molecular oxygen. Such energy absorption is normally observed as a result of increase of the molecular gas flow fraction in the mixture ($O_2 + e^{hot} \rightarrow O_2^v + e^{cold}$, where O_2^v denotes vibrationally the excited O_2 molecule).[58]

Finally Figs. 9(c) and 9(d) represent the behavior of selected Ar and O emission lines, reflecting the population of the corresponding excited atomic states in plasma (shown in the legend). In both cases, these data reveal a hysteresis behavior, of which the line intensity significantly increases during the metallic-to-poisoned mode transition, which is consistent with literature.[34] This effect which can be already observed in Fig. 5, is rather predictable (i) since the Ar-dominated sputtering defines the space change at the end of the plasma pulse in poisoned mode, where also a higher level of Ar excitation can be expected (see Fig. 5), and (ii) due to the jump of the reactive gas partial pressure during this transition, also resulting in O_2 dissociation leading to a higher O production and excitation. It should also be noted that all the other excited states of Ar ($2p_1$ through $2p_8$) and O ($3p\ ^5P_{3,2,1}$ and $3p\ ^3P_{0,2,1}$) demonstrate qualitatively the same behavior during the transition to poisoned mode, whereas the metallic emission lines drop during this transition (as verified separately), one more time confirming the described tendencies in the reactive HiPIMS plasma during the mode transitions.

IV. CONCLUSIONS

The results of this work demonstrate various trends in the ground state atomic number densities of the reactive gas (O in our case) and sputtered neutrals (Ti) and ions (Ti^+) in reactive HiPIMS discharge. The time-resolved changes of the O density in the HiPIMS afterglow, as well as the changes of all the studied atomic densities induced by variation of the plasma pulse energy indicate the existence of few different mechanisms of the ground state O atom production in the discharge. Among them, the electron impact dissociation of O_2 and the sputtered compounds in the ionization region (such as TiO, TiO_2 in the case of Ti target), along with direct O sputtering are likely the most probable outcomes. The role of Ar metastables in the O production during the afterglow should also be important, but the relative contribution of this process needs a separate verification.

The studies related to the hysteresis effects in reactive HiPIMS show that in the poisoned mode, the O atom density is clearly detectable both using OES (during the plasma pulse) and TALIF (during the afterglow) techniques. In the metallic mode, however, TALIF technique gives the O atom density values close to (or below) the detection limit, estimated to be around 10^{12} cm^{-3} in our case. Most of the studied discharge parameters, such as the number densities of O, Ti, Ti^+, and Ar^{met} atoms, O dissociation degree, discharge peaks current and voltage, as well as the plasma emission clearly reveals a hysteresis-like behavior. In the case of electron temperature, this effect is less evident, and vanishingly small for the Ti ionization degree.

The found behavior for Ti neutrals and ions, as well as for Ti ionization degree demonstrates a strong (more than a tenfold) decrease of the metal atom densities as a result of the metallic-to-poisoned mode transition, being in a good agreement with the previous studies. The hysteresis behavior for the O ground state atoms, detected for the first time in HiPIMS, is also in a perfect agreement with the well-known Berg's model of reactive sputtering.[14,18] At the same time, the proper estimation of the O_2 dissociation degree (probably also time- and space-resolved) requires an extended future research involving the local *in-situ* (likely laser-based) measurements assisted by the corresponding density calibration techniques. The trends in O_2 dissociation found so far show a monotonous decay in the poisoned mode, presumably as a

result of the combined decrease in Ar^{met} density, electron density, and electron temperature as a result of the O_2 addition.

Apart from showing the absolute densities for the sputtered and reactive atomic species in reactive HiPIMS discharge, as well as their dynamics during the hysteresis process, the results of this work should be useful for further kinetic modeling of HiPIMS discharges as well as for simulation of the film growth for the sake of understanding of the surface chemistry, stoichiometry control, etc.

ACKNOWLEDGMENTS

This work is supported by the Belgian Government through the "Pôle d'Attraction Interuniversitaire" (PAI, P7/34, "Plasma-Surface Interaction," Ψ). N.B. acknowledges the support of the "REFORGAS GreenWin" Project (Grant No. 7267). S.K. is the research associate of the National Foundation for Scientific Research (FRS—FNRS, Belgium). A.B. thanks the University of West Bohemia in Plzeň for support under the Project Nos. SGS-2016-056 and INTER-16. T.S. was partially supported by the Portuguese FCT, under the Project Nos. UID/FIS/50010/2013 and PTDC/FIS-PLA/1420/2014.

[1]D. V. Mozgrin, I. K. Fetisov, and G. V. Khodachenko, Plasma Phys. Rep. **21**, 400 (1995).
[2]I. K. Fetisov, I. V. Ivanov, G. V. Khodachenko, D. V. Mozgrin, D. B. Petrov, A. M. Snegirev, and T. V. Shukshina, J. Phys. Conf. Ser. **207**, 012021 (2010).
[3]I. K. Fetisov, A. A. Filippov, G. V. Khodachenko, D. V. Mozgrin, and A. A. Pisarev, Vacuum **53**, 133 (1999).
[4]V. Kouznetsov, K. Macák, J. M. Schneider, U. Helmersson, and I. Petrov, Surf. Coat. Technol. **122**, 290 (1999).
[5]J. T. Gudmundsson, Vacuum **84**, 1360 (2010).
[6]U. Helmersson, M. Lattemann, J. Bohlmark, A. P. Ehiasarian, and J. T. Gudmundsson, Thin Solid Films **513**, 1 (2006).
[7]J. T. Gudmundsson, N. Brenning, D. Lundin, and U. Helmersson, J. Vac. Sci. Technol. A Vac., Surf., Film **30**, 030801 (2012).
[8]S. Konstantinidis, J. P. Dauchot, and M. Hecq, Thin Solid Films **515**, 1182 (2006).
[9]K. Sarakinos, J. Alami, and S. Konstantinidis, Surf. Coat. Technol. **204**, 1661 (2010).
[10]N. Britun, T. Minea, S. Konstantinidis, and R. Snyders, J. Phys. D: Appl. Phys. **47**, 224001 (2014).
[11]J. T. Gudmundsson, Plasma Phys. Controlled Fusion **58**, 014002 (2016).
[12]N.-W. Pi, M. Zhang, J. Jiang, A. Belosludtsev, J. Vlček, J. Houška, and E. I. Meletis, Thin Solid Films **619**, 239 (2016).
[13]J. Musil, P. Baroch, J. Vlček, K. H. Nam, and J. G. Han, Thin Solid Films **475**, 208 (2005).
[14]S. Berg and T. Nyberg, Thin Solid Films **476**, 215 (2005).
[15]D. Horwat and A. Anders, J. Appl. Phys. **108**, 123306 (2010).
[16]M. Palmucci, N. Britun, S. Konstantinidis, and R. Snyders, J. Appl. Phys. **114**, 113302 (2013).
[17]M. Aiempanakit, A. Aijaz, D. Lundin, U. Helmersson, and T. Kubart, J. Appl. Phys. **113**, 133302 (2013).
[18]S. Berg, H. Blom, T. Larsson, and C. Nender, J. Vac. Sci. Technol. A **5**, 202 (1987).
[19]D. Depla, *Magnetrons, Reactive Gases and Sputtering*, 3rd ed. (Diederik Depla, Ghent, 2015).
[20]T. Kubart, D. Depla, D. M. Martin, T. Nyberg, and S. Berg, Appl. Phys. Lett. **92**, 221501 (2008).
[21]J. Schulte and G. Sobe, Thin Solid Films **324**, 19 (1998).
[22]S. Berg, E. Särhammar, and T. Nyberg, Thin Solid Films **565**, 186 (2014).
[23]K. Sarakinos, J. Alami, C. Klever, and M. Wuttig, Surf. Coat. Technol. **202**, 5033 (2008).
[24]T. Kubart, M. Aiempanakit, J. Andersson, T. Nyberg, S. Berg, and U. Helmersson, Surf. Coat. Technol. **205**, S303 (2011).
[25]N. Britun, M. Palmucci, S. Konstantinidis, and R. Snyders, J. Appl. Phys. **117**, 163302 (2015).
[26]N. Britun, J. G. Han, and S.-G. Oh, Plasma Sources Sci. Technol. **17**, 045013 (2008).
[27]N. Britun, J. G. Han, and S.-G. Oh, Appl. Phys. Lett. **92**, 141503 (2008).
[28]E. Wallin and U. Helmersson, Thin Solid Films **516**, 6398 (2008).
[29]D. Lundin, M. Čada, and Z. Hubička, J. Vac. Sci. Technol. A Vac., Surf., Film **34**, 041305 (2016).
[30]D. Benzeggouta, M. C. Hugon, J. Bretagne, and M. Ganciu, Plasma Sources Sci. Technol. **18**, 045025 (2009).
[31]M. Aiempanakit, T. Kubart, P. Larsson, K. Sarakinos, J. Jensen, and U. Helmersson, Thin Solid Films **519**, 7779 (2011).
[32]M. Palmucci, S. Konstantinidis, and R. Snyders, in *ISSP-2013 Int'l Conference Proceedings*, Kyoto (2013), p. 197.
[33]M. Audronis, V. Bellido-Gonzalez, and B. Daniel, Surf. Coat. Technol. **204**, 2159 (2010).
[34]M. Audronis and V. Bellido-Gonzalez, Surf. Coat. Technol. **205**, 3613 (2011).
[35]N. Britun, A. Belosludtsev, T. Silva, and R. Snyders, J. Phys. D: Appl. Phys. **50**, 075204 (2017).
[36]N. Britun, M. Palmucci, S. Konstantinidis, and R. Snyders, J. Appl. Phys. **117**, 163303 (2015).
[37]K. Niemi, V. S. Der Gathen, and H. F. Döbele, J. Phys. D: Appl. Phys. **34**, 2330 (2001).
[38]Q. Xiong, H. Liu, N. Britun, A. Y. Nikiforov, L. Li, Q. Chen, and C. Leys, IEEE Trans. Plasma Sci. **44**, 2745 (2016).
[39]T. Silva, N. Britun, T. Godfroid, and R. Snyders, Plasma Sources Sci. Technol. **23**, 025009 (2014).
[40]V. N. Ochkin, *Spectroscopy of Low Temperature Plasma* (Wiley-VCH, Weinheim, 2009).
[41]J. B. Boffard, R. O. Jung, C. C. Lin, and A. E. Wendt, Plasma Sources Sci. Technol. **19**, 065001 (2010).
[42]See www.lxcat.net for Biagi Database; accessed 29 July 2016.
[43]R. Payling and P. Larkins, *Optical Emission Lines of the Elements (CD-ROM)* (Wiley & Sons Inc., New York, 2000).
[44]See http://physics.nist.gov/PhysRefData/ASD/lines_form.html for NIST Atomic Spectra Database Lines Form.
[45]T. Silva, N. Britun, T. Godfroid, J. van der Mullen, and R. Snyders, J. Appl. Phys. **119**, 173302 (2016).
[46]D. Depla, S. Heirwegh, S. Mahieu, J. Haemers, and R. De Gryse, J. Appl. Phys. **101**, 013301 (2007).
[47]N. Britun, S. Konstantinidis, and R. Snyders, Plasma Processes Polym. **12**, 1010 (2015).
[48]C. Vitelaru, D. Lundin, N. Brenning, and T. Minea, Appl. Phys. Lett. **103**, 104105 (2013).
[49]J. T. Gudmundsson, D. Lundin, N. Brenning, M. A. Raadu, C. Huo, and T. M. Minea, Plasma Sources Sci. Technol. **25**, 065004 (2016).
[50]C. Nouvellon, M. Michiels, J. P. Dauchot, C. Archambeau, F. Laffineur, E. Silberberg, S. Delvaux, R. Cloots, S. Konstantinidis, and R. Snyders, Surf. Coat. Technol. **206**, 3542 (2012).
[51]J. Bohlmark, J. Alami, C. Christou, A. P. Ehiasarian, and U. Helmersson, J. Vac. Sci. Technol. A Vac., Surf., Film **23**, 18 (2005).
[52]A. Hecimovic and A. P. Ehiasarian, J. Phys. D: Appl. Phys. **42**, 135209 (2009).
[53]J. Vlcek, A. D. Pajdarova, and J. Musil, Contrib. Plasma Phys. **44**, 426 (2004).
[54]D. Darwent, Natl. Stand. Ref. Data Ser. Natl. Bur. Stand. **31**, 9 (1970).
[55]J. T. Gudmundsson, D. Lundin, G. D. Stancu, N. Brenning, and T. M. Minea, Phys. Plasmas **22**, 113508 (2015).
[56]A. Pajdarová, J. Vlček, P. Kudláček, and J. Lukáš, Plasma Sources Sci. Technol. **18**, 025008 (2009).
[57]P. Poolcharuansin and J. W. Bradley, Plasma Sources Sci. Technol. **19**, 025010 (2010).
[58]N. Britun, M. Gaillard, A. Ricard, Y. M. Kim, K. S. Kim, and J. G. Han, J. Phys. D: Appl. Phys. **40**, 1022 (2007).